Electronic Supplementary Material (ESI) for Journal of Materials Chemistry A.
This journal is © The Royal Society of Chemistry 2022

Supporting Information

Controlling domain size to enhance piezoelectricity of $BiFeO_3$-$BaTiO_3$ via heterovalent doping

Lixu Xie[1)], Mingyue Mo[1)], Hao Chen[1)], Yining Xie[1)], Yuan Cheng[1)], Chongrui Shu[1)], Qiang Chen[1)], Jie Xing[1)], Zhi Tan[1),*], Jianguo Zhu[1),*] and Huixiang Zhu[2)]

1) *College of Materials Science and Engineering, Sichuan University, 610064 Chengdu, China*

2) *Guangzhou Kailitech Electronics Co., Ltd, Guangzhou 511356, China*

1.1 Calculation detail

All the calculations are carried out by the Vienna ab initio simulation package (VASP)[1, 2] which is based on density functional theory (DFT) and the plane-wave pseudopotential methods. The SCAN meta-GGA exchange correlation function is used in present work [3], which is proved to generate high accuracy for most ferroelectrics. The plane-wave cutoff energy is set at 520 eV and the convergence for energy is chosen as 10^{-6}eV. The structural optimization is obtained until the Hellmann-Feynman forces acting on each atom is less than 0.01eV/Å. The valence electron configurations considered in the calculation are Bi ($5d^{10}6s^26p^3$), Fe ($3s^23p^63d^64s^2$), and O ($2s^22p^4$), respectively. A $\sqrt{2} \times \sqrt{2} \times \sqrt{2}$ rhombohedral cell contained 10 atoms with an angle round 60° is used to conduct the calculations. Rock-salt G-typed antiferromagnetic (AFM) order is assumed for all calculations, as well as a homogeneous and collinear spin arrangement. The first Brillouin zone (BZ) is sampled by a 7×7×7, Monkhorst-Pack mesh [4] of k points.

1.2 Relaxor characteristics

A typical relaxor ferroelectric may be separated into three areas ranging from low

*Corresponding authors: nic0400@scu.edu.cn and tanzhi0838@scu.edu.cn

to high temperature: nonergodic state (NE), ergodic state (E), and non-polar state[5-7]. Here, burn temperature T_B separates the non-polar and nonergodic regions, below which the dielectric response deviates from Curie-Weiss law and is accompanied by the appearance of dynamic polar nanoregions (PNRs). While freezing temperature T_f separates the nonergodic and nonergodic regions, below which the active PNRs and nanodomain rapidly become static ferroelectric domains. Obviously, the difference between nonergodic and ergodic lies mainly in the stability of the ferroelectric domains. The nanodomains of nonergodic-ferroelectric (NE-RFE) can be irreversibly poled into long-range ordered (LRO) ferroelectric domains and remain stable after poling; while the poling of PNRs in ergodic-ferroelectric (E-RFE) is reversible and recovers rapidly after removing the applied field.

2. Results and discussion

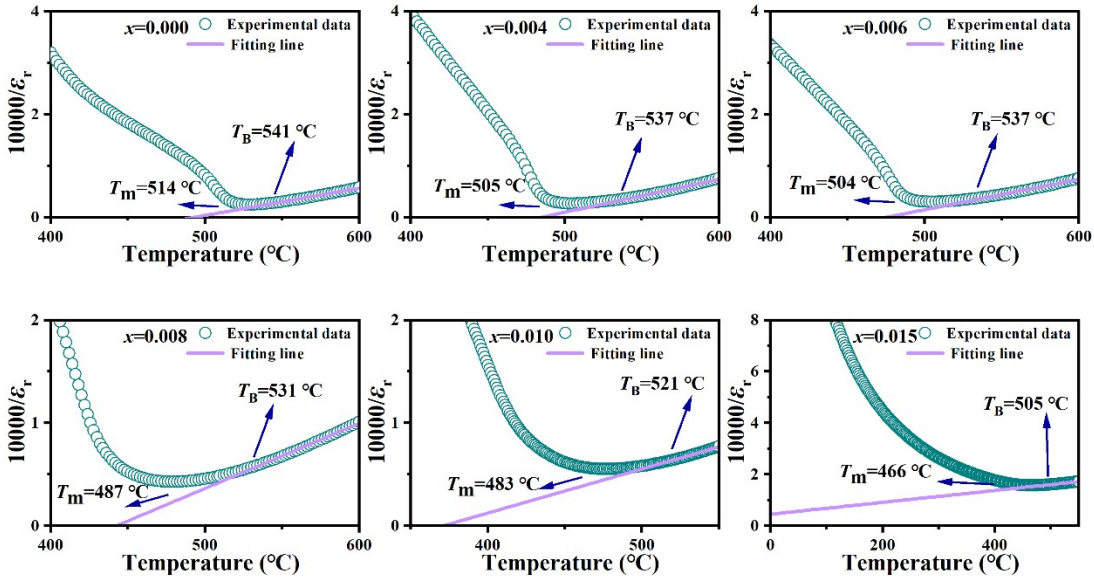

Fig. S1. The relationship of the T and ε_r of BF-BT-xNT ceramics with the vibration of

x

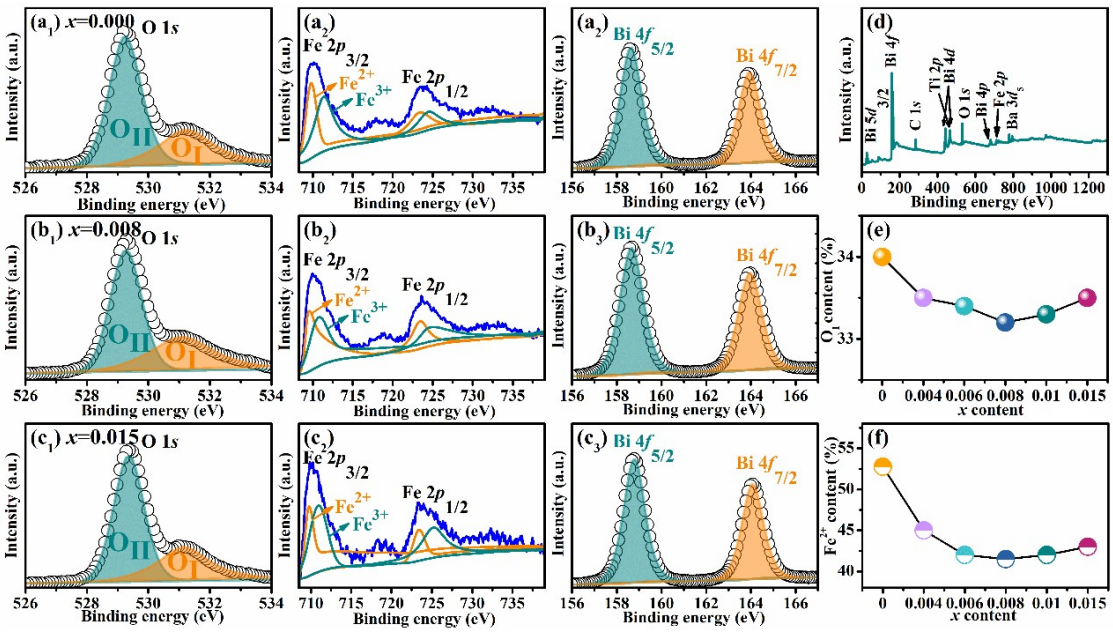

Fig. S2. X-ray photoelectron spectroscopy (XPS) spectra of BF-BT-*x*NT ceramics with (a_{1-3}) *x*=0.000, (c_{1-3}) *x*=0.008 and (c_{1-3}) *x*=0.015; statistics and analysis of BF-BT-*x*NT: (d) survey, (e) O_I content and (f) Fe^{2+} content with different *x*.

The X-ray photoelectron spectroscopy spectra are used to investigate the influence of $NaTaO_3$ doping on the states of elements in ceramics. Most elements may be detected in ceramics, as illustrated in Fig. S2(d). The high-resolution XPS spectra of Fe 2*p* is shown in Fig. S2(a_2), (b_2) and (c_2). The broad asymmetric peaks are Fe $2p_{3/2}$ and $2p_{1/2}$, indicating that Fe^{2+} and Fe^{3+} coexist[8, 9]. The O 1*s* spectra in Fig. S2(a_1), (b_1) and (c_1) may be loosely fitted into two peaks, O_I at 529.22 eV and O_{II} at 531.90 eV. O_I is frequently connected with lattice oxygen vacancies[8]. Moreover, Fig. S2(e) and (f) show how the content of Fe^{2+} and O_I varies doping of $NaTaO_3$. According to the aforementioned study, when $NaTaO_3$ enters the BF-BT ceramic lattice, the following happens at the B-site:

$$Ta_2O_5 + 2V_O^{\cdot\cdot} \xrightarrow{Fe_2O_{3(lattice)}\ B-site} 2Ta_{Fe}^{\cdot\cdot} + 5O_O^x\ , \qquad (1)$$

As it reports, Ta^{5+} and Mn^{4+} are beneficial in inhibiting the transition of Fe^{3+} to Fe^{2+}, thus the level of Fe^{2+} reduces when *x* increases [see Fig. S2(f)]. Simultaneously, Ta^{5+} doping helps to lower the concentration of oxygen vacancies, while the created B-site vacancies stimulate ion transport, resulting in grain growth and density improvement.

On the other hand, the following procedure may occur at the A-site:

$$Na_2O \xrightarrow{Bi_2O_{3(lattice)}\ A-site} 2Na_{Bi}^{''} + V_O^{\cdot\cdot} + O_O^x\ , \qquad (2)$$

$$4Na^+ + O_2 \xrightarrow{A-site} 2Na_2O\uparrow + 2V_O^{\cdot\cdot}\ , \qquad (3)$$

$$2Bi^{3+} + 3O_2 \xrightarrow{A-site} 2Bi_2O_3\uparrow + 3V_O^{\cdot\cdot}\ , \qquad (4)$$

Due to the non-stoichiometric ratio of 5% Bi excess, the entry of Na^+ into the A-site would compete with the excess Bi^{3+}. As a result, the amount of oxygen vacancies generated at A-site is smaller than that generated at B-site, resulting in a drop in the total oxygen vacancy concentration. However, since the boiling point of Na_2O (1275 °C) is substantially lower than that of Bi_2O_3 (1890 °C), the ions at the A-site would volatilize more during the sintering process, increasing the residual oxygen vacancies with a high level of Na^+ doping. Based on above process, when x grows, the content of oxygen vacancies first increases and subsequently reduces [see Fig. S2(e)].

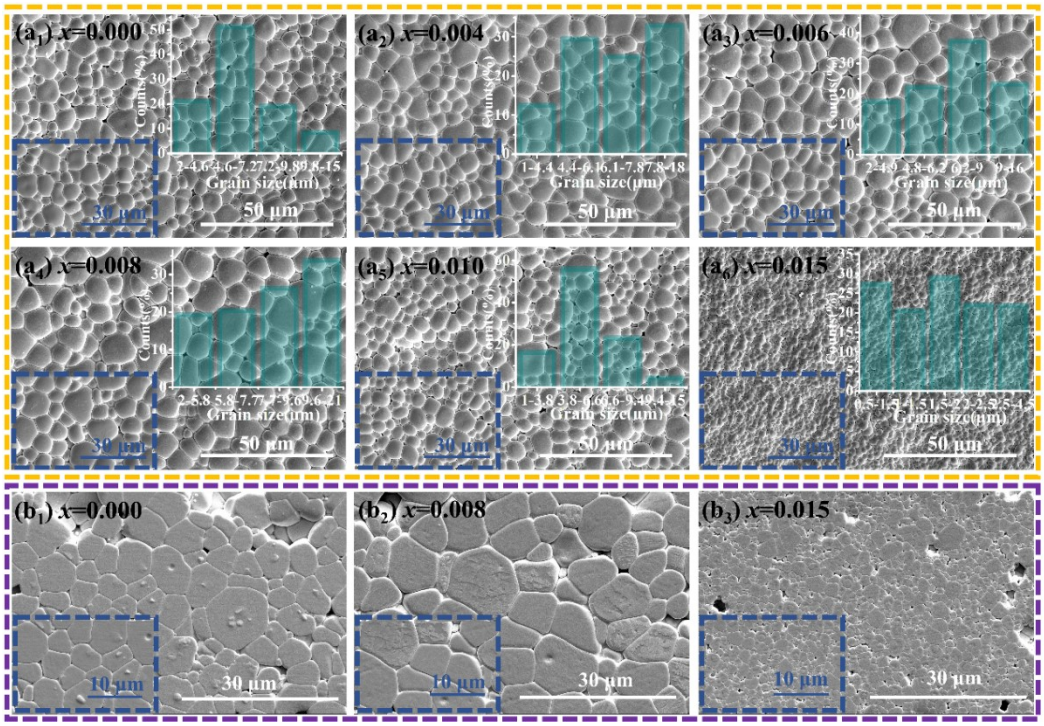

Fig. S3. SEM surface micrographs of the BF-BT-xNT ceramics with (a_1) x=0.000, (a_2) x=0.004, (a_3) x=0.006, (a_4) x=0.008, (a_5) x=0.010, (a_6) x=0.015; surface SEM images of the polished and thermally etched ceramics with (b_1) x=0.000, (b_2) x=0.010 and (b_3) x=0.015, the inset is an enlarged view.

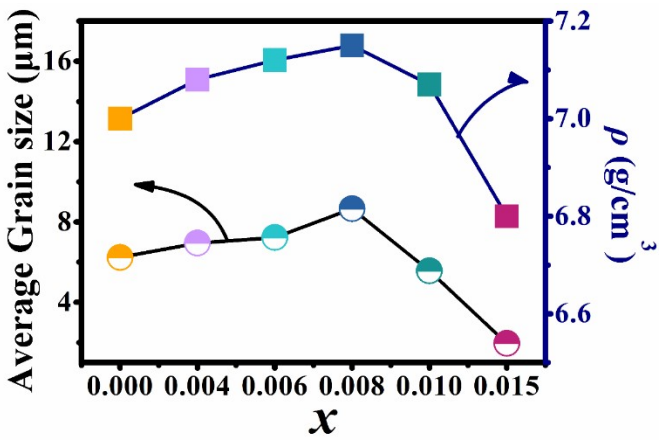

Fig. S4. Average grain size and density of BF-BT-*x*NT ceramics as a function of *x*.

SEM is employed to study the surface morphology of the ceramics, and three samples are chosen for polishing and thermal etching, as shown in Fig. S3(b). Although the ceramic is dense generally, there are visible macropores in the undoped component, and the grains grow dramatically with $NaTaO_3$ doping. The density of the ceramic increases significantly due to the filling of holes by tiny and medium grains, reaching a maximum value at x=0.008 [see Fig. S4(b_2)]. The fundamental reason for this is because the vacancies created by inequivalent elements promote ion transport and consequently grain growth. However, with the further increase of the amount of $NaTaO_3$ doping, the excessive doping leads to obvious grain refinement and the formation of a large number of pores, resulting in a substantial decrease in the average grain size and density (see Fig. S3 and Fig. S4)[10, 11].

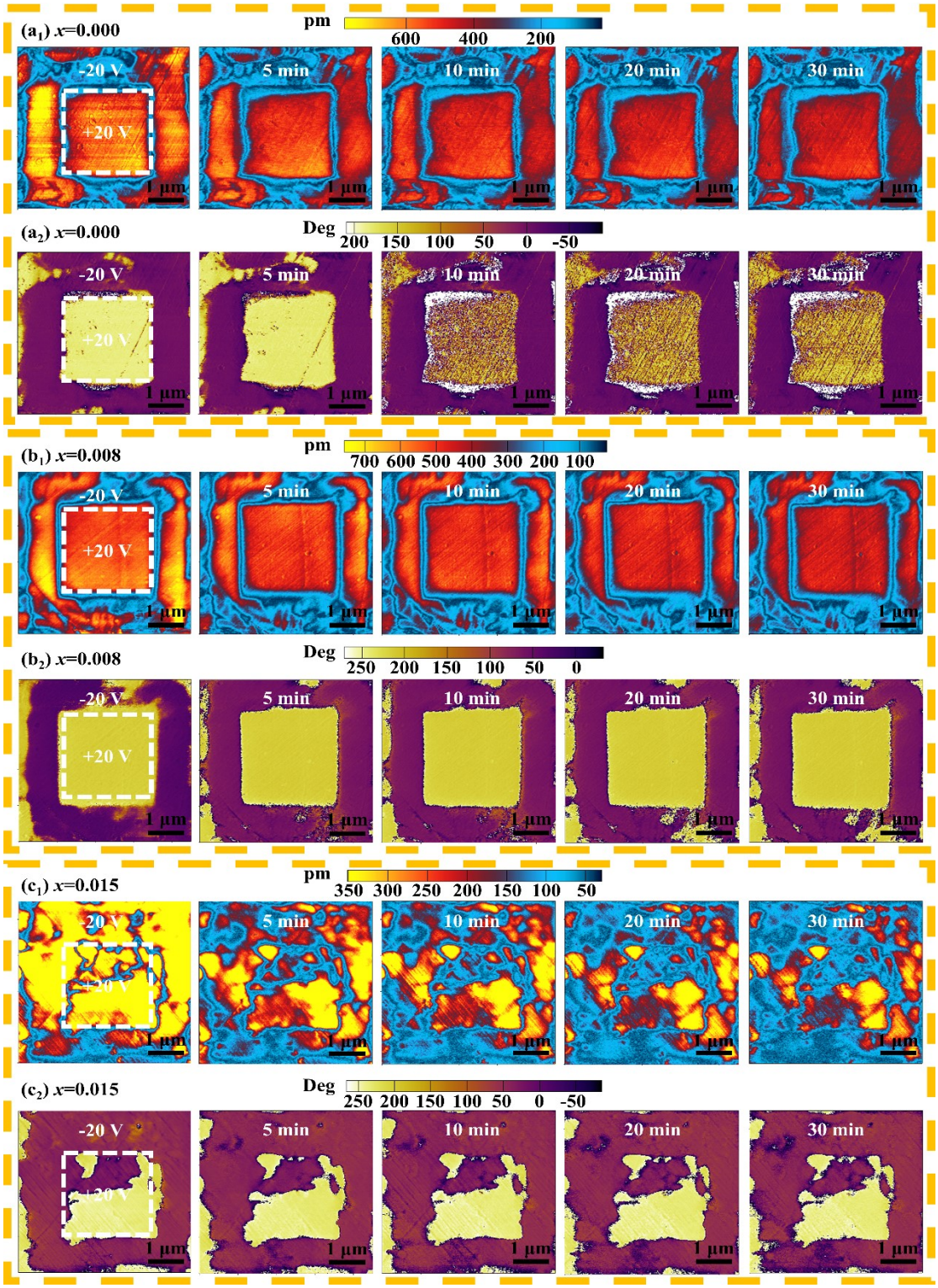

Fig. S5. After local poling (litho) of ceramics with (a) x=0.000, (b) x=0.008 and (c) x=0.015 using 20 V DC voltage: 2 V AC voltage is applied to record the domain morphology after the relaxation process (1, 5, 10, 15 and 30 min).

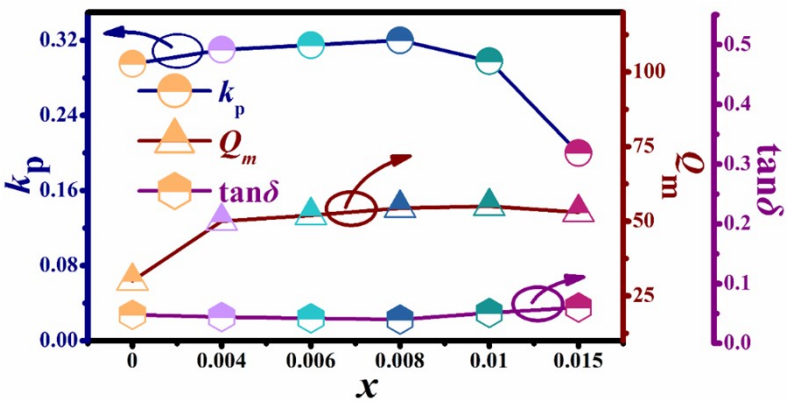

Fig. S6. Electromechanical coupling coefficient k_p, dielectric loss tanδ, and quality factor Q_m values as a function of x..

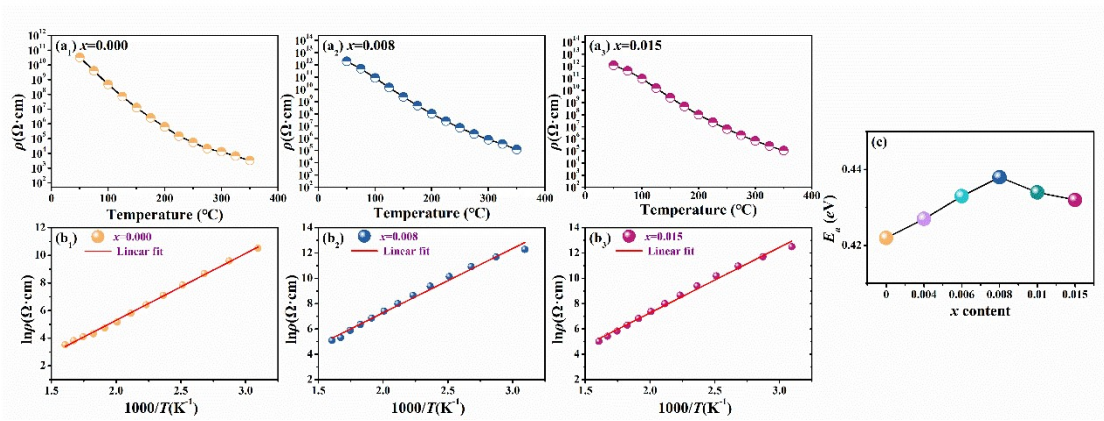

Fig. S7. ($a_{1\text{-}3}$) DC resistivity as a function of temperature; ($b_{1\text{-}3}$) line fitting between Lnρ vs. 1000/T to calculate the activation energy E_a; (c) Variation of activation energy E_a as function of x.

The thermal activation of defects and oxygen vacancies is widely understood to be intimately connected to domain wall motion and thermal depolarization during thermal treatment. DC resistivity is used to demonstrate how resistance varies with temperature from 50 to 350 °C. As seen in Fig. S7($a_{1\text{-}3}$), the DC resistivity values steadily drop from more than 10^{13} Ω·cm as temperature rises. Furthermore, since the DC resistivity follows the Arrhenius law, as Equation 5[12]:

$$\rho=\rho_0 \exp\left(\frac{E_a}{k_B T}\right) \qquad (5)$$

where ρ is the DC resistivity of the ceramic, T is the temperature, and E_a is the activation

energy of the charge carrier. The activation energies of all ceramics are fitted in Fig. S7(b_{1-3}) based on the linear connection between Ln ρ and $\frac{1}{T}$. The conductance activation energy increases and then falls with $NaTaO_3$ doping, as seen in Fig. S7(c), and its value is near to half of the second ionization energy of oxygen vacancies, which is the mixed conduction of ions and electrons[13, 14]. Since the secondary ionization energy of oxygen vacancies is mostly linked to their concentration, this finding correlates to a change in oxygen vacancy concentration in the XPS, implying that an adequate quantity of $NaTaO_3$ doping aids in improving the resistivity of BF-BT ceramics.

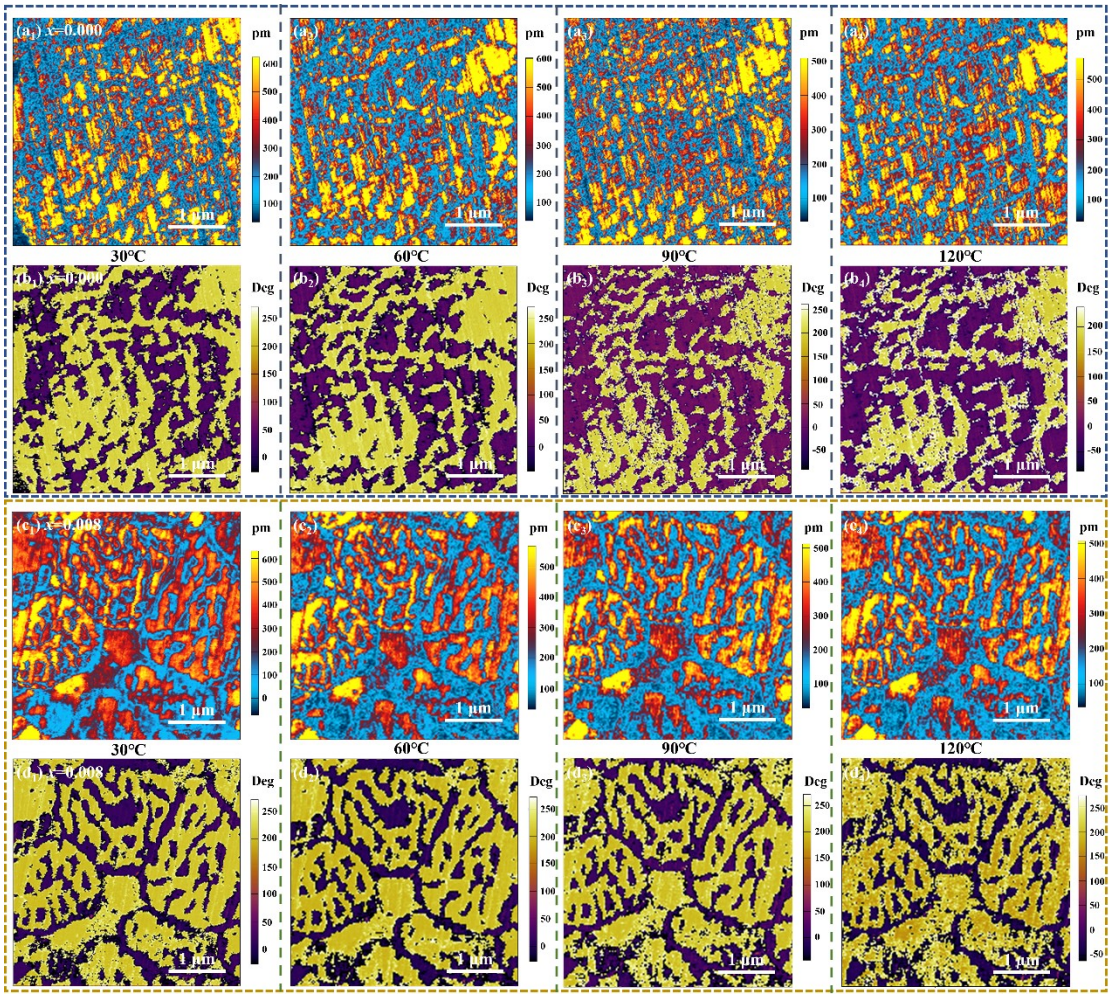

Fig. S8. Vertical piezoelectric force microscopy (VPFM) images information of ceramic with (a)(b) x=0.000 and (c)(d) x=0.08 at different temperature, including amplitude patterns and phase patterns

Table S1. Crystal structure parameters of the BF-BT-*x*NT ceramics derived from the Rietveld structure refinement program

Parameters	***x*=0.000**			***x*=0.004**			***x*=0.006**			***x*=0.008**			***x*=0.010**			***x*=0.015**		
Sig	1.38			1.59			1.54			1.95			1.82			1.88		
R_w(%)	3.362			3.93			3.92			4.18			4.6			4.74		
Symmetry	R phase	T phase	$Bi_{25}FeO_{40}$	R phase	T phase	$Bi_{25}FeO_{40}$	R phase	T phase	$Bi_{25}FeO_{40}$	R phase	T phase	$Bi_{25}FeO_{40}$	R phase	T phase	$Bi_{25}FeO_{40}$	R phase	T phase	$Bi_{25}FeO_{40}$
Space group	*R*3*c*	*P*4*mm*	*I*23	*R*3*c*	*P*4*mm*	*I*23	*R*3*c*	*P*4*mm*	*I*23	*R*3*c*	*P*4*mm*	*I*23	*R*3*c*	*P*4*mm*	*I*23	*R*3*c*	*P*4*mm*	*I*23
Phase ratio	64.53%	30.46%	5.01%	49.79%	45.18%	5.03%	44.42%	50.56%	5.02%	39.26%	55.76%	4.98%	37.43%	58.73%	3.84%	33.13%	63.01%	4.86%
a(Å)	5.632	3.996		5.632	3.994		5.632	3.993		5.631	3.990		5.630	3.990		5.629	3.989	
c(Å)	13.884	4.036		13.876	4.035		13.868	4.033		13.856	4.031		13.848	4.028		13.837	4.025	

Table S2. Oxygen octahedron parameters for BF-BT-*x*NT ceramics

Parameters	***x*=0.000**		***x*=0.004**		***x*=0.006**		***x*=0.008**		***x*=0.010**		***x*=0.015**	
Space group	*R*3*c*	*P*4*mm*	*R*3*c*	*P*4*mm*	*R*3*c*	*P*4*mm*	*R*3*c*	*P*4*mm*	*R*3*c*	*P*4*mm*	*R*3*c*	*P*4*mm*
Fe-O_A (Å)	1.9515	2.0243	1.9535	2.0136	1.9547	2.0134	1.9525	2.0097	1.9536	2.0092	1.9541	2.0089
Fe-O_B (Å)	2.136	2.0284	2.1261	2.015	2.1273	2.0116	2.1232	2.0093	2.1236	2.0078	2.124	2.0079
Fe-O_c (Å)	1.9515	1.9992	1.9535	1.9963	1.9547	1.9946	1.9525	1.996	1.9536	1.9949	1.954	1.993
Fe-O_D (Å)	2.1359	1.9953	2.1261	1.9975	2.1273	1.9964	2.1232	1.9974	2.1237	1.9959	2.124	1.9942
Fe-O_E (Å)	2.136	1.9944	2.1261	1.996	2.1273	1.9964	2.1232	1.9972	2.1237	1.9955	2.124	1.994
Fe-O_F (Å)	1.9515	1.9983	1.9535	1.9948	1.9547	1.9946	1.9525	1.9957	1.9536	1.9945	1.954	1.9928
∠O_A-Fe-O_B (°)	166.882	179.7	167.276	179.88	167.276	179.877	167.283	179.912	167.301	179.841	167.303	179.867
∠O_C-Fe-O_E (°)	166.882	179.937	167.276	179.816	167.276	179.876	167.284	179.834	167.301	179.896	167.303	179.889
∠O_D-Fe-O_F (°)	166.882	179.924	167.276	179.895	167.276	179.874	167.284	179.847	167.301	179.913	167.303	179.896
Tilting Angle (°)	10.65	-	10.0855	-	10.0855	-	10.0835	-	10.1040	-	10.1050	-

Table S3. Crystal structure parameters of the BF-BT-0.008NT ceramics derived from the Rietveld structure refinement program with different temperature

Temperature	Sig	R_w (%)	Symmetry	Space group	Phase ratio	*a* (Å)	*c* (Å)	*α* (°)
25 ℃	1.47	8.31	R phase	*R*3*c*	40.49%	5.6410	13.8250	
			T phase	*P*4*mm*	54.51 %	3.9920	4.0169	
			$Bi_{25}FeO_{40}$	*I*23	5.0%			
	1.65	9.20	R phase	*R*3*m*	44.20%	3.9801		89.8515
			T phase	*P*4*mm*	51.82%	3.9909	4.0117	
			$Bi_{25}FeO_{40}$	*I*23	3.98%			
100 ℃	1.53	8.52	R phase	*R*3*c*	44.75%	5.6480	13.8302	
			T phase	*P*4*mm*	52.38%	3.9951	4.0171	
			$Bi_{25}FeO_{40}$	*I*23	4.87%			
	1.58	8.98	R phase	*R*3*m*	48.63%	3.9845		89.8698
			T phase	*P*4*mm*	49.02%	3.9939	4.0132	
			$Bi_{25}FeO_{40}$	*I*23	4.35%			
200 ℃	1.57	8.94	R phase	*R*3*c*	50.97%	5.6519	13.8417	
			T phase	*P*4*mm*	46.72%	3.9981	4.0175	
			$Bi_{25}FeO_{40}$	*I*23	5.31%			
	1.53	8.58	R phase	*R*3*m*	49.98%	3.9881		89.8820
			T phase	*P*4*mm*	46.01%	3.9977	4.0141	
			$Bi_{25}FeO_{40}$	*I*23	4.01%			
			R phase	*R*3*c*	51.76%	5.6544	13.8510	

			T phase	*P*4*mm*	43.23%	4.0016	4.0176	
			$Bi_{25}FeO_{40}$	*I*23	5.01%			
	1.51	8.64	R phase	*R*3*m*	50.98%	3.9948		89.9222
			T phase	*P*4*mm*	44.64%	4.0013	4.0160	
			$Bi_{25}FeO_{40}$	*I*23	4.38%			
350 ℃	1.60	9.25	R phase	*R*3*c*	52.73%	5.6597	13.8690	
			T phase	*P*4*mm*	42.98%	4.0030	4.01816	
			$Bi_{25}FeO_{40}$	*I*23	4.29%			
	1.49	8.52	R phase	*R*3*m*	53.19%	3.9977		89.9296
			T phase	*P*4*mm*	41.78%	4.0030	4.0172	
			$Bi_{25}FeO_{40}$	*I*23	5.03			
400 ℃	1.62	9.40	R phase	*R*3*c*	57.57%	5.6640	13.8769	
			T phase	*P*4*mm*	37.62%	4.0041	4.0220	
			$Bi_{25}FeO_{40}$	*I*23	4.81%			
	1.53	8.61	R phase	*R*3*m*	55.24%	3.9977		89.9296
			T phase	*P*4*mm*	39.14%	4.0054	4.0181	
			$Bi_{25}FeO_{40}$	*I*23	4.81%			
	1.32	7.56	R phase	*R*3*m*	51.58%	4.0051		89.9742
			C phase	*Pm*3*m*	43.89%	4.0052		
			$Bi_{25}FeO_{40}$	*I*23	4.53%			
450 ℃	1.35	7.70	R phase	*R*3*m*	40.29%	4.0069	89.9902	
			C phase	*Pm*3*m*	55.21%	4.0057		

			$Bi_{25}FeO_{40}$	*I*23	4.5%			
500 °C	1.64	9.43	C phase	*Pm*3*m*	95.12%	4.0084		
			$Bi_{25}FeO_{40}$	*I*23	4.88%			

References:

1. G. Kresse and J. Furthmüller, *Phys. Rev. B*, 1996, **54**, 11169.
2. G. Kresse and J. Furthmüller, *Comput. Mater. Sci.*, 1996, **6**, 15-50.
3. J. Sun, A. Ruzsinszky and J. P. Perdew, *Phys. Rev. Lett.*, 2015, **115**, 036402.
4. H. J. Monkhorst and J. D. Pack, *Phys. Rev. B*, 1976, **13**, 5188.
5. L. Wu, X. Wang and L. Li, *RSC Adv.*, 2016, **6**, 14273-14282.
6. Z. Yang, H. Du, L. Jin, Q. Hu, H. Wang, Y. Li, J. Wang, F. Gao and S. Qu, *J. Mater. Chem. A*, 2019, **7**, 27256-27266.
7. X. Dong, X. Li, X. Chen, J. Wu and H. Zhou, *Chem. Eng. J.*, 2021, **409**.
8. B. Xun, N. Wang, B. Zhang, X. Chen, Y. Zheng, W. Jin, R. Mao and K. Liang, *Ceram. Int.*, 2019, **45**, 24382-24391.
9. T. Zheng, Y. Ding and J. Wu, *RSC Adv.*, 2016, **6**, 90831-90839.
10. Y. Xie, J. Xing, Z. Tan, L. Xie, Y. Cheng, X. Wu, R. Han, Q. Chen and J. Zhu, *Ceram. Int.*, 2022, **48**, 6565-6573.
11. J. Xing, Z. Tan, L. Xie, L. Jiang, J. Yuan, Q. Chen, J. Wu, W. Zhang, D. Xiao and J. Zhu, *J. Am. Ceram. Soc.*, 2018, **101**, 1632-1645.
12. B. Li, T. Zheng and J. Wu, *ACS Appl. Mater. Interfaces*, 2021, **13**, 37422-37432.
13. J. Yuan, R. Nie, Q. Chen, D. Xiao and J. Zhu, *Mater. Res Bull.*, 2019, **115**, 70-79.
14. T. Mondal, S. Das, T. Badapanda, T. P. Sinha and P. M. Sarun, *Physica B Condens. Matter.*, 2017, **508**, 124-135.